J Nanostruct 16(4): 4943-4963, Autumn 2026

RESEARCH PAPER

# Synthesis, Spectroscopic Characterization, and DFT/TD-DFT Investigation of a Novel Nano-Sized Azo Dye Ligand Derived from 2-Amino-6-methoxybenzothiazole and Its Pt(IV) Nano-Complex

*Sura A. Alsharaa [1]*, Khalid J. Al-Adilee [1], Entidhar K. Sahib [2], Ivan Farhan Jawad [2]*

[1] *Department of Chemistry, College of Science, University of AL-Qadisiyah, Diwaniya 1753, Iraq*

[2] *Department of Chemistry, College of Education, University of AL-Qadisiyah, Diwaniya, Iraq*

## ARTICLE INFO

***Article History:***
*Received 17 May 2026*
*Accepted 06 August 2026*
*Published 01 October 2026*

***Keywords:***
*6-methoxybenzothiazole*
*Azo dye*
*DFT/TD-DFT*
*Nanoparticles*
*Pt(IV) nano-complex*

## ABSTRACT

A novel tridentate azo dye ligand, 2-[2′-(6-methoxybenzothiazolyl) azo]-3,4-dimethylbenzoic acid (6-MBTAMB, $C_{17}H_{15}N_3O_3S$, MW = 341.39 g/mol), was synthesized through the diazotization of 2-amino-6-methoxybenzothiazole followed by coupling with 3,4-dimethylbenzoic acid under alkaline conditions. The ligand was coordinated with Pt(IV) chloride to yield a mononuclear nano-complex of the type $[Pt(L)Cl_3]\cdot H_2O$ ($C_{17}H_{16}Cl_3N_3O_4PtS$, MW = 659.84 g/mol). Both compounds were characterized by elemental analysis (C, H, N, S), UV-Vis and FT-IR spectroscopy, $^1$H-NMR, mass spectrometry, powder X-ray diffraction, and field-emission scanning electron microscopy (FESEM). FESEM analysis confirmed the nanoscale morphology of both the ligand and the Pt(IV) complex, with average particle sizes of 68.89 nm and 40.50 nm, respectively. XRD analysis corroborated these findings, yielding average crystallite sizes of 29.25 nm for the ligand and 21.71 nm for the nano-complex via the Debye–Scherrer equation. Spectroscopic evidence confirmed tridentate (N,N,O) coordination through the thiazole nitrogen, one azo nitrogen, and the carboxylate oxygen, affording an octahedral geometry around the $d^6$ Pt(IV) center. The free ligand was also examined by DFT at the B3LYP/3-21G level, which gave HOMO and LUMO energies of −5.9529 and −2.5220 eV (ΔE = 3.4309 eV) together with the Koopmans reactivity descriptors and the Mulliken charge distribution. A TD-DFT run placed the strongest calculated absorption at $\lambda_{max}$ = 328.1 nm (f = 0.3919), a band of π→π* character. Taken together, the experimental and computed results describe the electronic structure of this heterocyclic azo dye system, its coordination behavior toward Pt(IV), and the nanoscale character of the resulting platinum(IV) complex.

**How to cite this article**
*Alsharaa S., Al-Adilee K, Sahib E., Jawad I. Synthesis, Spectroscopic Characterization, and DFT/TD-DFT Investigation of a Novel Nano-Sized Azo Dye Ligand Derived from 2-Amino-6-methoxybenzothiazole and Its Pt(IV) Nano-Complex. J Nanostruct, 2026; 16(4):4943-4963. DOI: 10.22052/JNS.2026.04.040*

* *Corresponding Author Email: sura.ali.abdalhassan@qu.edu.iq*

## INTRODUCTION

Roughly 60% of all industrially produced dyes are azo dyes; some surveys put the share closer to 70% [1]. No other class of synthetic colorant comes close. The name refers to the –N=N– unit joining two aromatic or heteroaromatic rings, and this bridge is also the chromophore: conjugation through it gives strong bands throughout the visible region. Textile work is only part of the story now. A benzothiazole, benzimidazole or pyridine ring attached to the azo group brings additional N and S donor atoms, and the dye then behaves as a multidentate chelator toward transition metals [2,3]. Reported applications for the resulting complexes include catalysis, drug candidates, treatment of contaminated water, chemical sensing and solar cells [4,5].

Interest has grown lately in metal complexes whose crystallites are of nanometer size. The bulk and nano forms of the same compound can behave quite differently. Small crystallites expose more surface, and quantum confinement together with surface effects alters the optical response; biological activity often improves as well [6]. Nano-sized azo dye complexes in particular have given good antimicrobial and anticancer results [7]. There is a practical difficulty, though: the particles like to agglomerate. Controlled preparation, followed by careful characterization, is therefore essential in this field [8].

Pt(IV) occupies a special position among the platinum-group ions. It is a $d^6$ ion, kinetically inert, and it takes six-coordinate octahedral geometry almost without exception. Pt(IV) prodrugs built on these properties are under study as replacements for cisplatin; oral dosing becomes possible and off-target toxicity drops [9]. Reports that combine Pt(IV) with benzothiazolyl azo dyes at the nanoscale are nevertheless rare, and calculations describing the electronic consequences of that combination are rarer. One cannot design such compounds rationally without knowing how charge moves across the –N=N– bridge from the heterocyclic donor to the metal [10].

DFT is the standard tool for questions of this sort. The frontier orbital energies give the ionization potential and the electron affinity at once; Koopmans' theorem turns them into electronegativity (χ), chemical hardness (η), softness (σ) and the electrophilicity index (ω), the usual global measures of reactivity [11]. TD-DFT handles the excited states, which lets one compare computed UV-Vis transitions with the recorded spectrum [12]. Mulliken population analysis assigns a charge to each atom, showing where donor–acceptor interactions will occur and which sites are most reactive [13]. Calculations of this kind, run beside the usual spectroscopic and morphological measurements, tell more about a new azo dye–metal system than either would on its own.

Here we describe a new tridentate azo dye, 2-[2′-(6-methoxybenzothiazolyl)azo]-3,4-dimethylbenzoic acid (6-MBTAMB), and the Pt(IV) nano-complex derived from it. The two compounds were characterized by elemental analysis, UV-Vis, FT-IR and $^1$H-NMR spectroscopy, mass spectrometry, powder XRD and FESEM imaging; special care was taken to establish that the prepared complex is indeed nano-dimensional. The experimental work is accompanied by a DFT/TD-DFT study of the free ligand at the B3LYP level covering the HOMO–LUMO energies, the reactivity descriptors, the Mulliken charges, the molecular electrostatic potential and a simulated absorption spectrum. Our aim was to connect the calculated electronic properties with what the spectra actually show, and in doing so to learn how a benzothiazolyl azo framework binds a heavy-metal center at the nanoscale.

## MATERIALS AND METHODS

*Chemicals and Instrumentation*

Reagents were used as received. 2-Amino-6-methoxybenzothiazole, sodium nitrite ($NaNO_2$), hydrochloric acid, 3,4-dimethylbenzoic acid, potassium hexachloroplatinate(IV) ($K_2PtCl_6$) and the common solvents were analytical-grade materials (BDH/Aldrich). Electronic spectra were run in ethanol ($10^{-3}$ M) between 200 and 1100 nm on a Shimadzu UV-1800 spectrophotometer, and FT-IR spectra were taken from KBr discs on a Shimadzu IRAffinity-1 instrument over 4000–400 $cm^{-1}$. $^1$H-NMR measurements employed a Bruker 400 MHz spectrometer, with the samples in DMSO-$d_6$ and TMS as the internal standard. An Agilent 5975 GC-MS system supplied the mass spectra. Powder XRD patterns were collected on a Shimadzu XRD-6000 diffractometer with Cu Kα radiation (λ = 1.5406 Å) at a scan rate of 2° $min^{-1}$, and FESEM images were taken on a TESCAN MIRA3 field-emission scanning electron microscope to examine the morphology, particle size and surface features of the ligand and its Pt(IV) complex.

*Synthesis of the Azo Dye Ligand (6-MBTAMB)*

The ligand was obtained by the usual diazotization and coupling sequence [14,15]. A sample of 2-amino-6-methoxybenzothiazole (1.80 g, 10 mmol) was taken up, with gentle warming, in concentrated HCl (5 mL) diluted with deionized water (35 mL). After the solution had been cooled to 0–5 °C in an ice bath, a pre-cooled solution of $NaNO_2$ (0.69 g, 10 mmol in 10 mL $H_2O$) was run in dropwise over 15 min with stirring; the mixture was then held below 5 °C for a further 30 min to complete formation of the diazonium salt. Separately, 3,4-dimethylbenzoic acid (1.50 g, 10 mmol) was dissolved in NaOH solution (10 mL, 10%). The alkaline coupling component was added gradually to the diazonium solution with vigorous stirring at 0–5 °C. The resulting deep-orange precipitate was collected by filtration, washed thoroughly with cold water, and recrystallized from hot ethanol. Yield: 78%, m.p. 110–112 °C.

The synthetic route for the preparation of the azo dye ligand 6-MBTAMB is outlined in Fig. 1.

*Synthesis of the Pt(IV) Nano-Complex*

The Pt(IV) nano-complex was prepared by dissolving the ligand 6-MBTAMB (0.10 g, 0.29 mmol) in 20 mL of hot ethanol. This solution was added with stirring to a stoichiometric amount of $K_2PtCl_6$ dissolved in 20 mL ethanol. The resulting mixture was refluxed for 3 h at 78 °C with continuous stirring. The dark reddish-purple precipitate that formed was collected by filtration, washed with cold ethanol and diethyl ether, and dried in a vacuum desiccator. Yield: 76%, decomp. 190–192 °C. The non-electrolytic character was confirmed by a low molar conductance value ($\Lambda_m$ < 15 S cm² mol$^{-1}$ in DMF), ruling out ionic species [16]. The analytical data for both compounds are summarized in Table 1.

*Computational Details*

All quantum chemical calculations were performed using the PySCF program package (version 2.4) [17] interfaced with the RDKit cheminformatics toolkit for initial three-

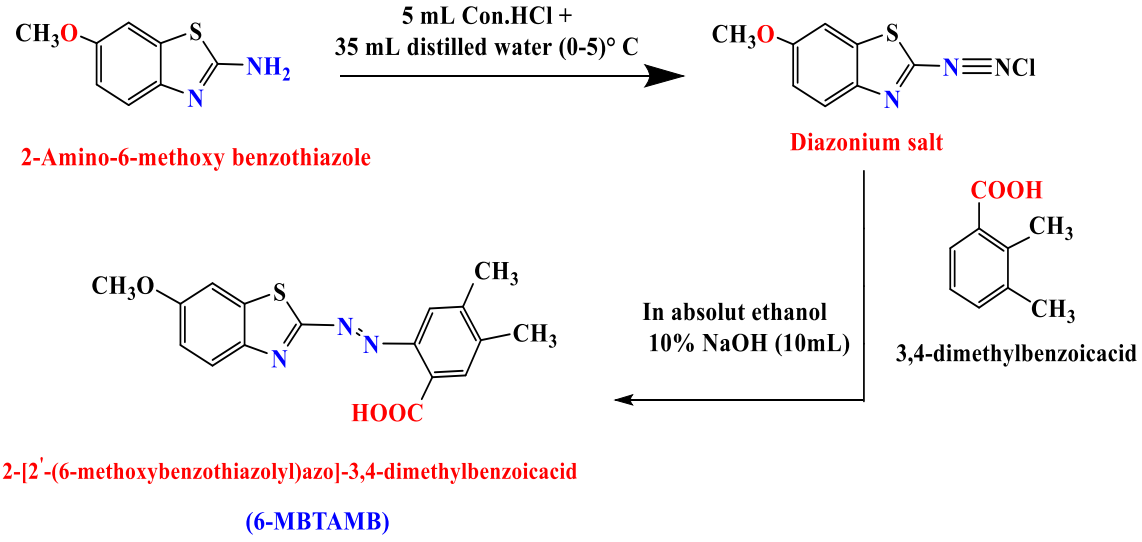


Fig. 1. Preparation of the ligand 2-[2′-(6-methoxybenzothiazolyl)azo]-3,4-dimethylbenzoic acid (6-MBTAMB) [14,15].

Table 1. Physical properties and analytical data of the azo dye ligand and of its Pt(IV) nano-complex; elemental analyses are listed as calculated (found) [14,15].

| Compound | Colour | m.p. (°C) | Yield (%) | M.f. (M.wt.) | C% | H% | N% | S% | M% |
|---|---|---|---|---|---|---|---|---|---|
| 6-MBTAMB (LH) | Reddish orange | 110–112 | 78 | $C_{17}H_{15}N_3O_3S$ (341.39) | 59.81 (60.19) | 4.43 (4.54) | 12.31 (12.82) | 9.39 (9.70) | – |
| $[Pt(L)Cl_3]\cdot H_2O$ | Reddish purple | 190–192 | 76 | $C_{17}H_{16}Cl_3N_3O_4PtS$ (659.84) | 30.95 (31.46) | 2.44 (2.54) | 6.37 (6.91) | 4.86 (5.25) | 29.56 (29.82) |

* Elemental analysis figures are quoted as calculated (found); M% refers to Pt. Molar conductance of the complex in DMF: Λm < 15 S cm² mol$^{-1}$ (non-electrolyte).

dimensional coordinate generation via the ETKDG algorithm followed by MMFF94 force-field pre-optimization. Ground-state electronic structure calculations for the free ligand employed the restricted Kohn–Sham (RKS) formalism with the B3LYP hybrid density functional and the 3-21G basis set (250 basis functions for 178 electrons) in the gas phase. The SCF procedure was converged to a threshold of $10^{-8}$ Hartree using the default DIIS algorithm with a maximum of 200 cycles. Frontier molecular orbital (FMO) energies were used to derive global reactivity descriptors via Koopmans' theorem [18]: ionization potential ($I = -E_{HOMO}$), electron affinity ($A = -E_{LUMO}$), electronegativity ($\chi = (I + A)/2$), chemical potential ($\mu = -\chi$), chemical hardness ($\eta = (I - A)/2$), chemical softness ($\sigma = 1/2\eta$), electrophilicity index ($\omega = \chi^2/2\eta$), and maximum charge transfer index ($\Delta N_{max} = -\mu/\eta$).

Mulliken population analysis was performed on the converged SCF density to quantify atomic charge distribution. Time-dependent DFT (TD-DFT) calculations were carried out at the B3LYP/STO-3G level (139 basis functions) using the Tamm–Dancoff approximation (TDA) for the lowest 10 singlet excited states. Oscillator strengths were computed in the dipole-length gauge. The molecular electrostatic potential (MEP) surface was constructed from the Mulliken charge distribution projected onto the molecular framework. Throughout, the molecule was treated as a neutral closed-shell singlet (charge = 0, spin = 0), the appropriate ground state for the free ligand [19].

*Determination of Nanoscale Structural Parameters*

Crystallographic quantities were derived from the powder XRD patterns by the standard routes. Bragg's law (Eq. 1) gave the interplanar spacings; the volume-weighted mean crystallite size D came from the Debye–Scherrer equation (Eq. 2); the dislocation density δ followed from the Williamson–Smallman relation (Eq. 3); and the lattice microstrain ε was estimated with the tangent formula (Eq. 4):

$$n\lambda = 2d \sin\theta \quad (1)$$

$$D = K\lambda / (\beta \cos\theta) \quad (2)$$

$$\delta = 1 / D^2 \quad (3)$$

$$\varepsilon = \beta / (4 \tan\theta) \quad (4)$$

Here λ = 1.5406 Å (Cu Kα), K = 0.9, β is the FWHM of the reflection in radians and θ is the Bragg angle. Each observed reflection was treated separately; the tables list D and δ per line together with their arithmetic means [29,30,52]. For the FESEM sizes we measured at least 50 well-resolved particles per image in ImageJ and report the arithmetic mean [33].

## RESULTS AND DISCUSSION

*Elemental Analysis and Physical Properties*

Analytical and physical data appear in Table 1. 6-MBTAMB forms reddish-orange crystals, m.p. 110–112 °C, in 78% yield. The Pt(IV) product is a reddish-purple powder obtained in 76% yield; it shows no melting point and decomposes at 190–192 °C instead. The gap between the two temperatures is large, roughly 80 degrees, and it reflects what coordination does here: Pt–N and Pt–O bonds lock the ligand into an octahedral frame that resists heating far better than the free molecule.

Microanalysis matches the proposed formulae for both compounds. Ligand $C_{17}H_{15}N_3O_3S$ (MW = 341.39 g/mol): C, 59.81 (60.19); H, 4.43 (4.54); N, 12.31 (12.82); S, 9.39 (9.70). Complex $C_{17}H_{16}Cl_3N_3O_4PtS$ (MW = 659.84 g/mol): C, 30.95 (31.46); H, 2.44 (2.54); N, 6.37 (6.91); S, 4.86 (5.25); Pt, 29.56 (29.82). Platinum is the decisive figure. Found 29.82% versus calculated 29.56%: a 1:1 metal-to-ligand ratio, with one lattice water included in the formula, reproduces it almost exactly [14,15]. The found C and N values sit a little above the calculated ones, within the ±0.5–1.0% tolerance customary for heterocyclic azo compounds.

*Molar Conductance Measurements*

The complex was dissolved in DMF ($10^{-3}$ M) and its molar conductance read at room temperature. We measured $\Lambda_m < 15$ S cm² mol$^{-1}$. Non-electrolytes fall below $\Lambda_m < 30$ S cm² mol$^{-1}$, so the compound gives off no ions in solution [16]. This result confirms that all three chloride ligands are coordinated directly to the Pt(IV) center within the inner coordination sphere, rather than existing as dissociated counter-ions. The non-electrolytic nature is fully consistent with the proposed neutral molecular formula $[Pt(L)Cl_3]\cdot H_2O$, in which the water molecule occupies a lattice position outside the coordination sphere and the ligand coordinates as a monoanionic tridentate (N,N,O)

donor after deprotonation of the carboxylic acid group.

*Magnetic Susceptibility Measurements*

The magnetic susceptibility of the Pt(IV) nano-complex was measured at room temperature (Table 2). The complex exhibited diamagnetic behavior (μeff = 0 B.M.), consistent with a $d^6$ low-spin electronic configuration in which all six electrons are paired in the $t_2g$ set of orbitals under the influence of the strong octahedral ligand field. This observation is characteristic of Pt(IV) complexes, where the large crystal field splitting energy (Δoct) of the 5d orbitals invariably produces a low-spin arrangement [21,49]. The diamagnetic nature, combined with the electronic spectral data discussed in Section 3.4, supports the assignment of an octahedral geometry with $d^2sp^3$ hybridization at the platinum center in the nano-complex.

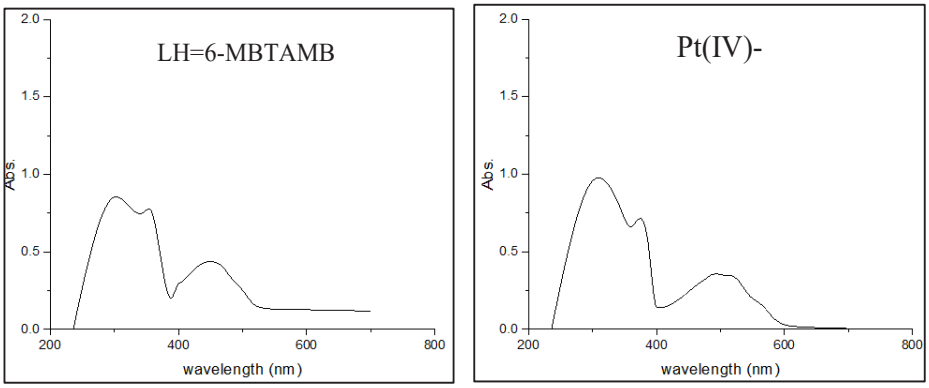


Fig. 2. UV-visible spectra of the benzothiazolyl azo ligand (6-MBTAMB) and its Pt(IV) nano-complex.

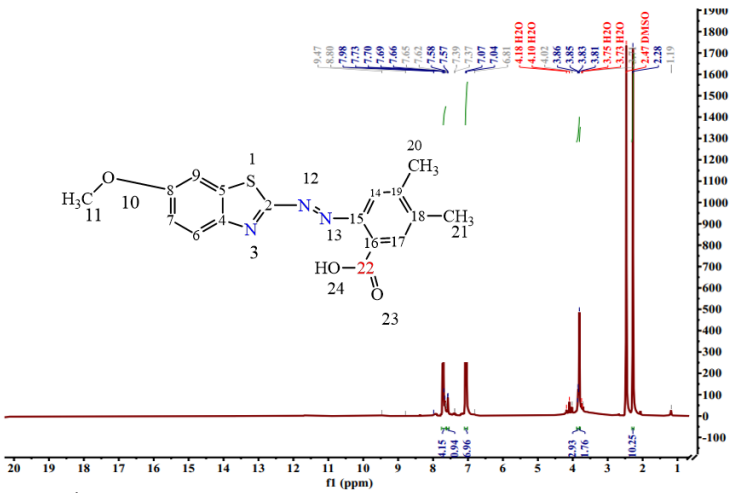


Fig. 3. $^1$H-NMR spectrum of the free azo ligand 6-MBTAMB recorded in DMSO-$d_6$.

Table 2. Electronic spectra, magnetic measurements, and proposed geometry of the nano-complex.

| Compound | λmax (nm) | Bands ($cm^{-1}$) | Transition | μeff (B.M.) | Geometry | Hybridization |
|---|---|---|---|---|---|---|
| 6-MBTAMB | 451 | 22173 | n→π* | – | – | – |
| 6-MBTAMB | 328 | 30488 | π→π* | – | – | – |
| $[Pt(L)Cl_3]\cdot H_2O$ | 496 | 20576 | $^1A_1g \rightarrow {}^1T_1g(F)$ | Dia | Octahedral | $d^2sp^3$ |
| $[Pt(L)Cl_3]\cdot H_2O$ | 441 | 22676 | $^1A_1g \rightarrow {}^1T_2g(F)$ | Dia | Octahedral | $d^2sp^3$ |
| $[Pt(L)Cl_3]\cdot H_2O$ | 348 | 28736 | $^1A_1g \rightarrow {}^1T_1g(P)$ | Dia | Octahedral | $d^2sp^3$ |

*Electronic Absorption Spectra*

In ethanol, the free ligand 6-MBTAMB shows two absorption bands (Table 2, Fig. 2). The higher-energy band at 328 nm (30488 $cm^{-1}$) belongs to the π→π* transition of the conjugated aromatic and heterocyclic framework. The second band, at 451 nm (22173 $cm^{-1}$), arises from the n→π* transition of the azo (–N=N–) group; it is this absorption that gives the free ligand its reddish-orange color [20].

For the Pt(IV) nano-complex, three bands appear, at 496 nm (20576 $cm^{-1}$), 441 nm (22676 $cm^{-1}$) and 348 nm (28736 $cm^{-1}$). We assign them to the d–d transitions $^1A_1g \rightarrow {}^1T_1g(F)$, $^1A_1g \rightarrow {}^1T_2g(F)$ and $^1A_1g \rightarrow {}^1T_1g(P)$, the pattern expected of a $d^6$ ion held in an octahedral ligand field. Together with the diamagnetism of the compound, these assignments point to low-spin octahedral Pt(IV) with $d^2sp^3$ hybridization [21]. The ligand bands themselves move to longer wavelength on complexation, a bathochromic shift that we put down to extended conjugation and to charge transfer between the ligand π-system and the platinum center in the nano-complex.

*$^1$H-NMR Spectral Analysis*

Fig. 3 shows the $^1$H-NMR spectrum of the ligand. The carboxylic acid proton (–COOH) gives a signal at δ = 9.47 ppm; it vanishes on shaking with $D_2O$, as a labile proton should. Aromatic protons of the benzothiazole unit fall as a multiplet between

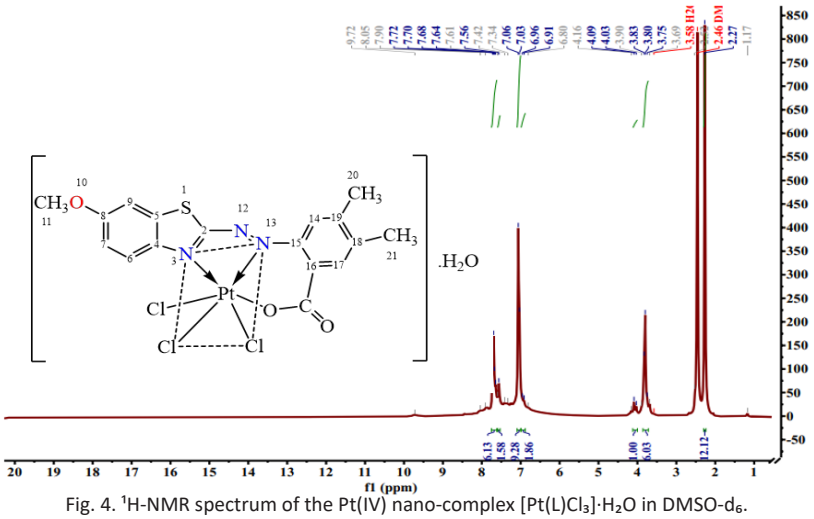


Fig. 4. $^1$H-NMR spectrum of the Pt(IV) nano-complex $[Pt(L)Cl_3]\cdot H_2O$ in DMSO-$d_6$.

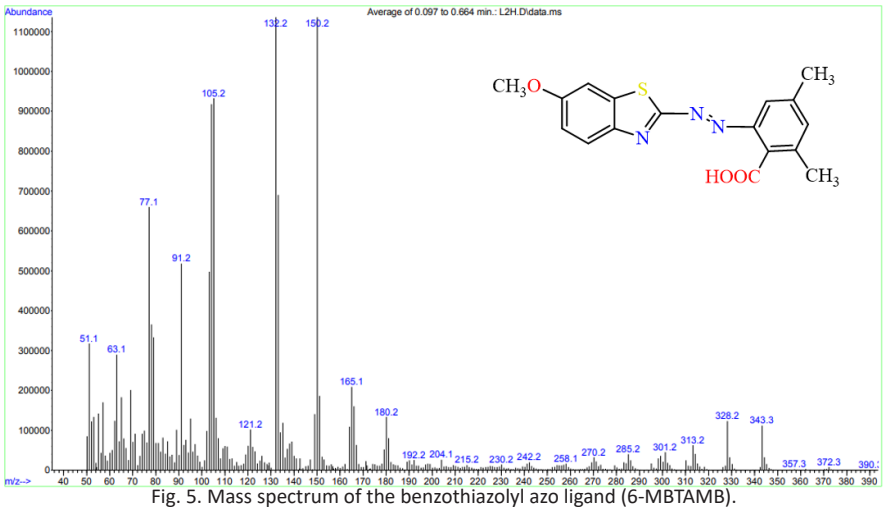


Fig. 5. Mass spectrum of the benzothiazolyl azo ligand (6-MBTAMB).

δ = 7.72 and 6.91 ppm. The methoxy group (–$OCH_3$) resonates at δ = 3.85 ppm, and the two ring methyls of the benzoic acid fragment appear as singlets at δ = 2.27 and 2.32 ppm [22].

Fig. 4 shows the complex. Aromatic protons again appear between δ = 7.72 and 6.91 ppm, now displaced a little downfield; the metal deshields nearby protons on coordination. The –COOH line changes more: it broadens and moves to higher frequency, the behavior expected once the carboxylate oxygen is bound to platinum. Lattice water announces itself as a new broad signal at δ = 3.33 ppm. Methyl and methoxy resonances are essentially where they were in the free ligand, so neither group takes part in metal coordination [23].

*Mass Spectrometry*

6-MBTAMB gives its molecular ion at m/z = 343 $[M+2]^+$ (Fig. 5), in accord with the formula $C_{17}H_{15}N_3O_3S$ and a molecular weight of 341.39 g/mol. Fragments at m/z = 328 $[M–CH_3]^+$, 301 and 192 record the stepwise loss of substituents; the base peak, at m/z = 149, comes from the benzothiazolyl fragment. This breakdown route is the one normally seen for heterocyclic azo compounds (Fig. 6, Table 3) [24].

For the Pt(IV) nano-complex the molecular ion appears at m/z = 603 $[M–Cl–2H_2O]^+$ (Fig. 7). Successive losses of chloride, water and pieces

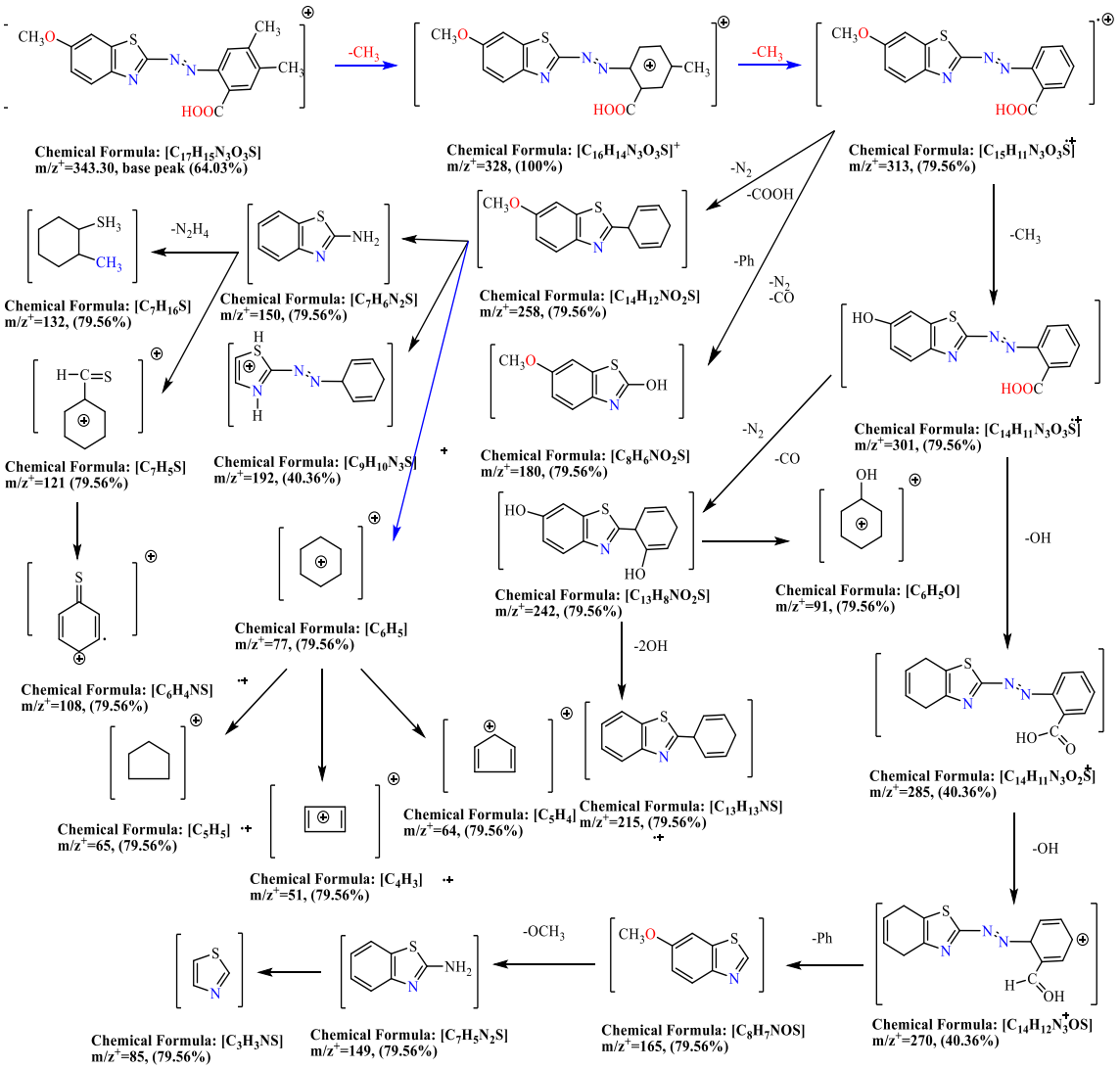


Fig. 6. Proposed mass fragmentation pathways for the benzothiazolyl azo ligand (6-MBTAMB).

of the organic ligand account for the remaining peaks (Fig. 8, Table 3), and the pattern as a whole supports the proposed molecular formula and the 1:1 metal-to-ligand ratio [25].

*FT-IR Spectral Analysis*

The FT-IR spectra of the free ligand and its Pt(IV) nano-complex provide direct evidence for the coordination mode (Table 4, Figs. 9 and 10). In the

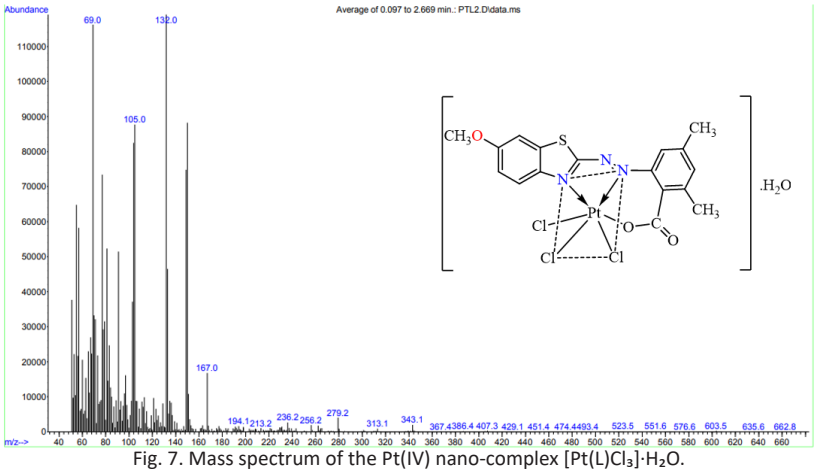


Fig. 7. Mass spectrum of the Pt(IV) nano-complex $[Pt(L)Cl_3]\cdot H_2O$.

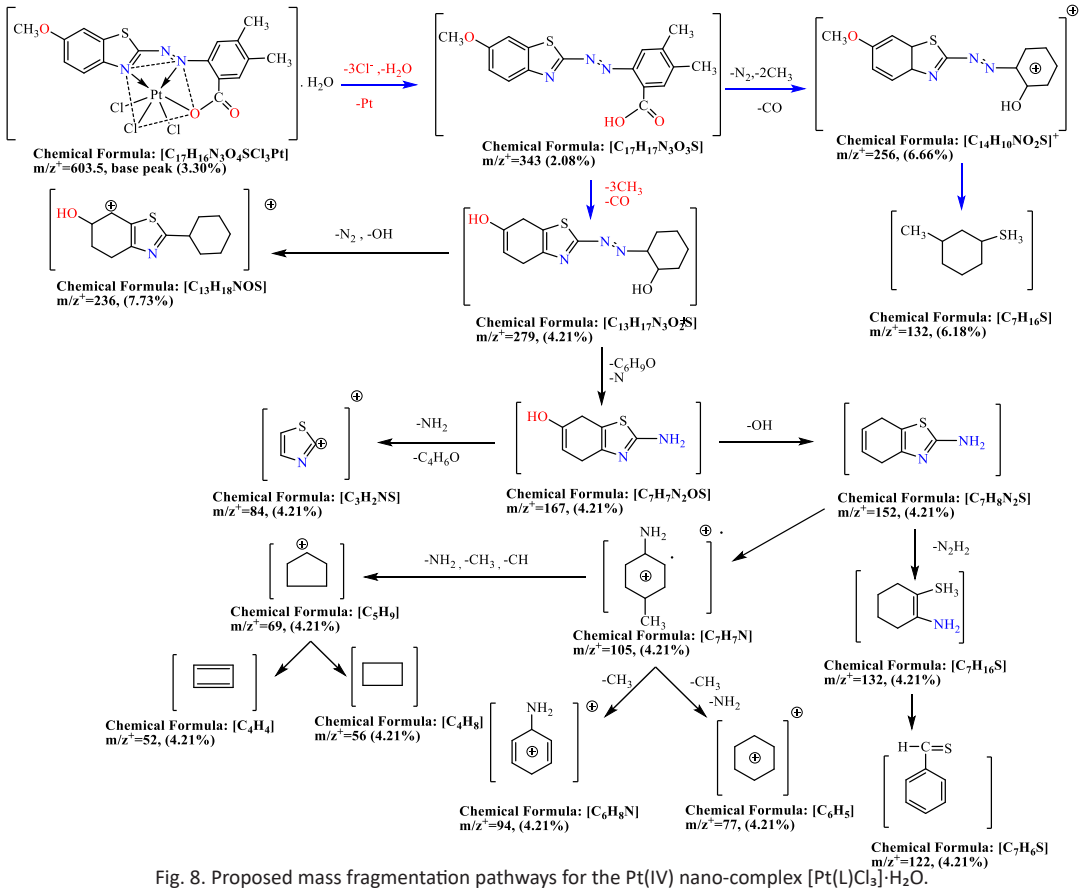


Fig. 8. Proposed mass fragmentation pathways for the Pt(IV) nano-complex $[Pt(L)Cl_3]\cdot H_2O$.

ligand spectrum, the broad band at 2834 $cm^{-1}$ is attributed to ν(O–H) of the carboxylic acid group. The ν(C=O) stretching vibration appears at 1689 $cm^{-1}$, and the thiazole ring ν(C=N) is observed at 1604 $cm^{-1}$. The azo bond ν(N=N) stretching frequency appears at 1490 $cm^{-1}$. Bands at 3088 and 2934 $cm^{-1}$ correspond to aromatic and aliphatic C–H stretching vibrations, respectively [26].

Upon formation of the Pt(IV) nano-complex, several diagnostic shifts are observed. A broad

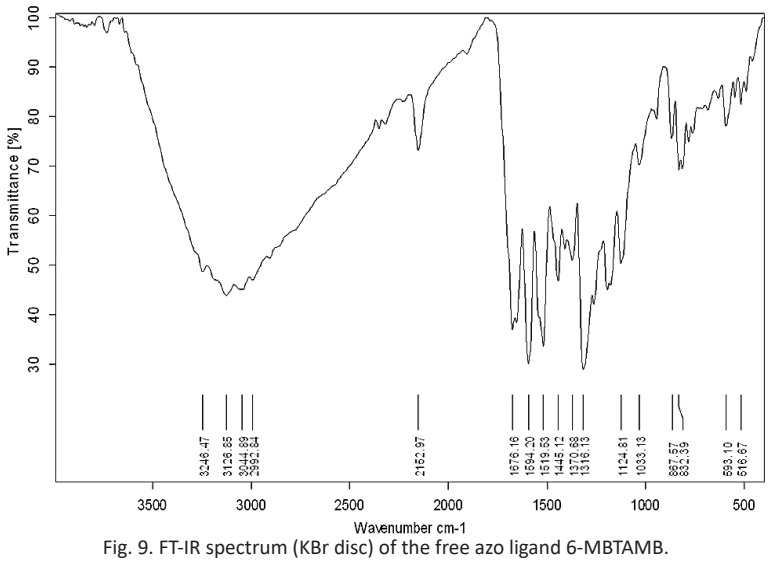


Fig. 9. FT-IR spectrum (KBr disc) of the free azo ligand 6-MBTAMB.

Table 3. Selected mass fragmentation data for the ligand and Pt(IV) nano-complex.

| 6-MBTAMB m/z⁺ | Fragment | Pt(IV)-Complex m/z⁺ | Fragment |
|---|---|---|---|
| 343 | $[C_{17}H_{15}N_3O_3S]^+$ | 603 | $[C_{17}H_{16}N_3O_4SCl_3Pt]$ |
| 328 | $[C_{16}H_{14}N_3O_3S]^+$ | 343 | $[C_{17}H_{17}N_3O_3S]$ |
| 301 | $[C_{14}H_{11}N_3O_3S]$ | 279 | $[C_{13}H_{17}N_3O_2S]$ |
| 192 | $[C_9H_{10}N_3S]^+$ | 167 | $[C_7H_7N_2OS]^+$ |
| 180 | $[C_8H_6NO_2S]$ | 152 | $[C_7H_8N_2S]$ |
| 149 | $[C_7H_5NS]^+$ | 105 | $[C_7H_7N]^+$ |
| 108 | $[C_6H_4S]^+$ | 77 | $[C_6H_5]^+$ |
| 77 | $[C_6H_5]^+$ | 52 | $[C_4H_4]^+$ |

Table 4. Diagnostic FT-IR bands ($cm^{-1}$) of the azo dye ligand and of its Pt(IV) nano-complex.

| Group | 6-MBTAMB | $[Pt(L)Cl_3]\cdot H_2O$ |
|---|---|---|
| ν(O–H) / ν($H_2O$) | 2834 w.br. | 3446 s.br.* |
| ν(C–H) Aromatic | 2973 w. | 2974 w. |
| ν(C–H) Aliphatic | 2934 w. | 2933 w. |
| ν(C=O) | 1689 s. | 1686 m. |
| ν(C=N) | 1604 m. | 1605 w. |
| ν($COO^-$) asym. | 1560 m. | 1563 w. |
| ν(N=N) | 1490 w. | 1486 w. |
| ν($COO^-$) sym. | 1404 w. | 1404 w. |
| ν(C=C) | 1271, 737 w. | 1274, 774 w. |
| ν(C–S) | 1228, 834 m. | 1230, 835 m. |
| ν(C–O) | 1174 m. | 1156 w. |
| ν(C–N) | 1057 w. | 1087 w. |
| ν(C–C) | 915 w. | 1023 w. |
| ν(M–N) | – | 517 w. |
| ν(M–O) | – | 441 w. |
| ν(M–Cl) | – | 400 w. |

* = ($H_2O$) outside the coordination sphere

band at 3446 $cm^{-1}$ corresponds to ν(O–H) of the lattice water molecule. The ν(C=O) band shifts from 1689 to 1686 $cm^{-1}$, and the ν(C=N) from 1604 to 1605 $cm^{-1}$, while the ν(N=N) shifts from 1490 to 1486 $cm^{-1}$. Asymmetric and symmetric $COO^-$ stretching bands appear at 1563 and 1404 $cm^{-1}$ in the complex. Critically, new bands at 517 $cm^{-1}$ and 441 $cm^{-1}$ are assigned to ν(Pt–N) and ν(Pt–O) stretching modes, confirming metal–ligand bond formation. A further band at 400 $cm^{-1}$ belongs to ν(Pt–Cl), as expected when three chloride ligands remain bound in the octahedral nano-complex [27,28].

*X-ray Powder Diffraction (XRD) Analysis*

Powder XRD patterns were recorded for solid 6-MBTAMB and for its Pt(IV) nano-complex, partly to check crystallinity and phase purity, and above all to measure the crystallite size (Table 5, Fig. 11). Both patterns contain sharp reflections; the compounds are therefore well-ordered crystalline solids. For every diffraction line the interplanar

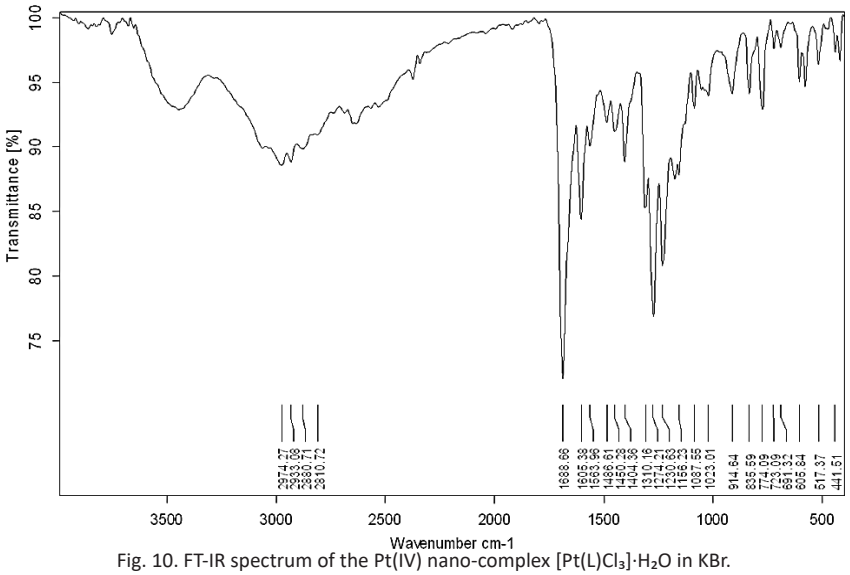


Fig. 10. FT-IR spectrum of the Pt(IV) nano-complex $[Pt(L)Cl_3]\cdot H_2O$ in KBr.

Table 5. Powder XRD data with the derived crystallite sizes, dislocation densities and lattice microstrain for the azo ligand and its Pt(IV) nano-complex.

| Compound | 2θ (°) | Height (cts) | FWHM (°) | d-spacing (Å) | Rel. Int. (%) | D (nm) | δ ($nm^{-2}$) | ε ($\times10^{-3}$) | Avg. D (nm) |
|---|---|---|---|---|---|---|---|---|---|
| 6-MBTAMB | 10.49 | 1786 | 0.197 | 8.432 | 37.68 | 41.97 | 0.000568 | 9.36 (avg. 6.66) | 29.25 |
| | 12.89 | 437 | 0.394 | 6.867 | 9.22 | 20.94 | 0.002281 | 15.22 | |
| | 15.25 | 3393 | 0.246 | 5.810 | 71.57 | 33.42 | 0.000895 | 8.02 | |
| | 21.25 | 1389 | 0.246 | 4.181 | 29.29 | 33.14 | 0.000911 | 5.72 | |
| | 23.65 | 1025 | 0.197 | 3.762 | 21.63 | 41.25 | 0.000588 | 4.11 | |
| | 25.29 | 4741 | 0.246 | 3.522 | 100.00 | 32.90 | 0.000924 | 4.78 | |
| | 26.20 | 1806 | 0.197 | 3.402 | 38.09 | 41.05 | 0.000593 | 3.69 | |
| | 28.53 | 663 | 0.295 | 3.129 | 13.98 | 27.23 | 0.001349 | 5.06 | |
| | 31.07 | 471 | 0.394 | 2.879 | 9.93 | 20.30 | 0.002426 | 6.18 | |
| | 38.14 | 158 | 0.590 | 2.359 | 3.33 | 13.28 | 0.005673 | 7.45 | |
| | 40.73 | 407 | 0.197 | 2.215 | 8.58 | 39.51 | 0.000641 | 2.32 | |
| | 43.29 | 395 | 0.246 | 2.090 | 8.33 | 31.34 | 0.001018 | 2.71 | |
| | 65.84 | 331 | 1.771 | 1.419 | 6.99 | 3.93 | 0.064720 | 11.94 | |
| Pt(IV) nano-complex | 12.92 | 418 | 0.295 | 6.854 | 54.86 | 27.92 | 0.001283 | 11.37 (avg. 11.58) | 21.71 |
| | 15.34 | 763 | 0.197 | 5.774 | 100.00 | 41.77 | 0.000573 | 6.38 | |
| | 21.16 | 372 | 0.295 | 4.199 | 48.79 | 27.62 | 0.001311 | 6.89 | |
| | 25.59 | 177 | 1.181 | 3.480 | 23.23 | 6.85 | 0.021314 | 22.69 | |
| | 66.12 | 170 | 1.574 | 1.413 | 22.24 | 4.42 | 0.051297 | 10.55 | |

spacing (d-spacing) was calculated from Bragg's law, $n\lambda = 2d \sin\theta$ [29].

Mean crystallite sizes came from the Debye–Scherrer equation, $D = K\lambda / \beta\cos\theta$, with $K = 0.9$ (shape factor), $\lambda = 1.5406$ Å (Cu Kα radiation), $\beta$ the full width at half maximum (FWHM) and $\theta$ the Bragg angle; the dislocation density $\delta = 1/D^2$ was evaluated as well, as a measure of lattice imperfection [30]. Both compounds turn out to be nanocrystalline. The free ligand averages D = 29.25 nm, and the Pt(IV) nano-complex averages a smaller D = 21.71 nm. Complexation therefore shrinks the coherent domains: a reasonable reading is that the bulky $PtCl_3$ unit interferes with the packing the organic molecule would otherwise adopt, leaving smaller nano-sized crystalline regions [31,32]. The dislocation density moves in the same direction, from $\delta = 6.36 \times 10^{-3}$ $nm^{-2}$ on average for the ligand to $\delta = 1.51 \times 10^{-2}$ $nm^{-2}$ for the complex, meaning the lattice of the complex carries more strain and disorder. In both compounds the crystallites measure well under 100 nm; the nano-crystalline description of the Pt(IV) complex is thus supported directly by the diffraction data.

Lattice microstrain was evaluated for each reflection from Eq. (4). Averaged over all observed lines, the free ligand exhibits $\varepsilon = 6.66 \times 10^{-3}$, whereas the Pt(IV) nano-complex shows a value almost twice as large, $\varepsilon = 1.16 \times 10^{-2}$. The simultaneous rise in microstrain and dislocation density on passing from the ligand to the complex is the expected signature of smaller and more defective coherent domains, and furnishes an independent, quantitative confirmation of the crystallite-size reduction inferred from the Scherrer

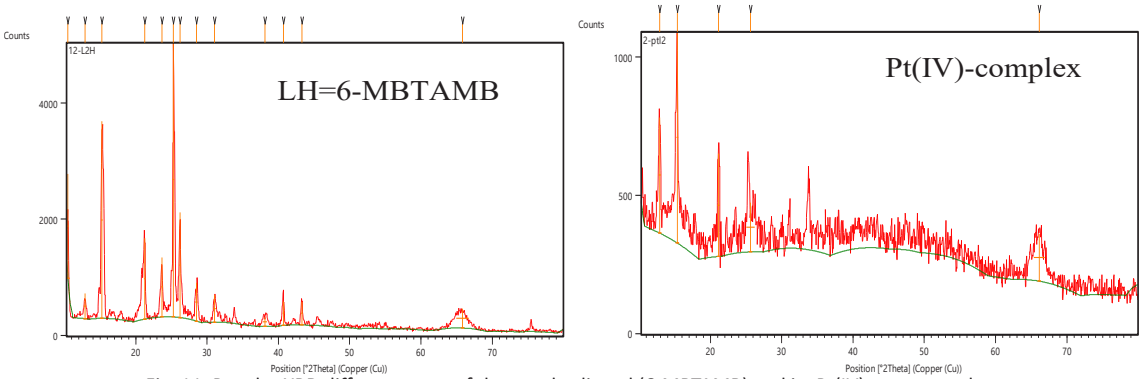


Fig. 11. Powder XRD diffractograms of the azo dye ligand (6-MBTAMB) and its Pt(IV) nano-complex.

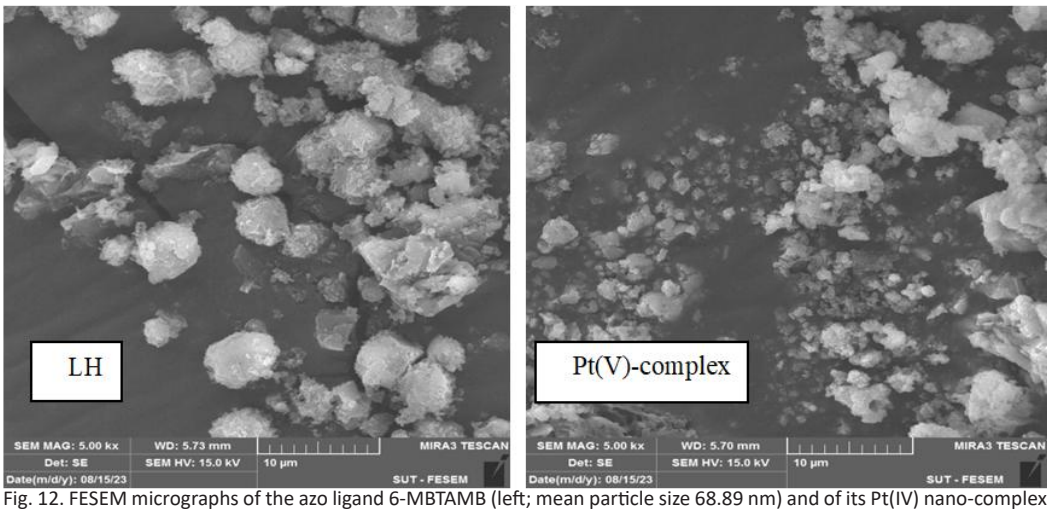


Fig. 12. FESEM micrographs of the azo ligand 6-MBTAMB (left; mean particle size 68.89 nm) and of its Pt(IV) nano-complex (right; mean 40.50 nm).

analysis [30,52]. It should be noted that the Debye–Scherrer treatment used here attributes the whole of the observed line broadening to size effects and does not deconvolute the instrumental contribution; the crystallite sizes in Table 5 are therefore lower-bound estimates, and the microstrain values are correspondingly upper-bound estimates [31,32,34].

*Field-Emission Scanning Electron Microscopy (FESEM)*

FESEM analysis was performed to evaluate the surface morphology, particle size distribution, and nanoscale features of the ligand and its Pt(IV) complex (Fig. 12). The surface properties of the compounds were studied in terms of particle dimensions, shape, and the degree of aggregation between neighboring crystallites, which are critical parameters for assessing nanoscale character [33].

The FESEM image of the benzothiazolyl azo ligand (6-MBTAMB) revealed agglomerated spherical crystalline nanoparticles with an average particle size of 68.89 nm. Its surface looks fairly smooth, and neighboring particles cling together to a moderate degree, much as one would expect where carboxylic acid and methoxy groups allow intermolecular hydrogen bonding. Even before complexation, then, the particle size of the free ligand sits well inside the nanoscale regime (< 100 nm) [34].

FESEM tells a different story for the complex. The particles are irregular rather than spherical, they aggregate less, the surface is more porous, and the mean size drops to 40.50 nm against 68.89 nm for the ligand. XRD had already recorded the same trend in the crystallites, 29.25 nm falling to 21.71 nm. One explanation covers both observations: the bulky $PtCl_3$ fragment gets in the way of the packing the free molecule prefers. Every size measured here is below 100 nm, which places both solids among nanostructured materials [35,36]. Small dimensions of this kind tend to raise surface reactivity, and often biological activity as well, compared with the bulk compound; follow-up biomedical and catalytic studies of the complex therefore seem worthwhile.

*DFT Computational Study of the Free Ligand Ground-State Energy and Convergence*

SCF convergence at B3LYP/3-21G presented no problems. The total electronic energy of the neutral closed-shell singlet came to −1437.1389

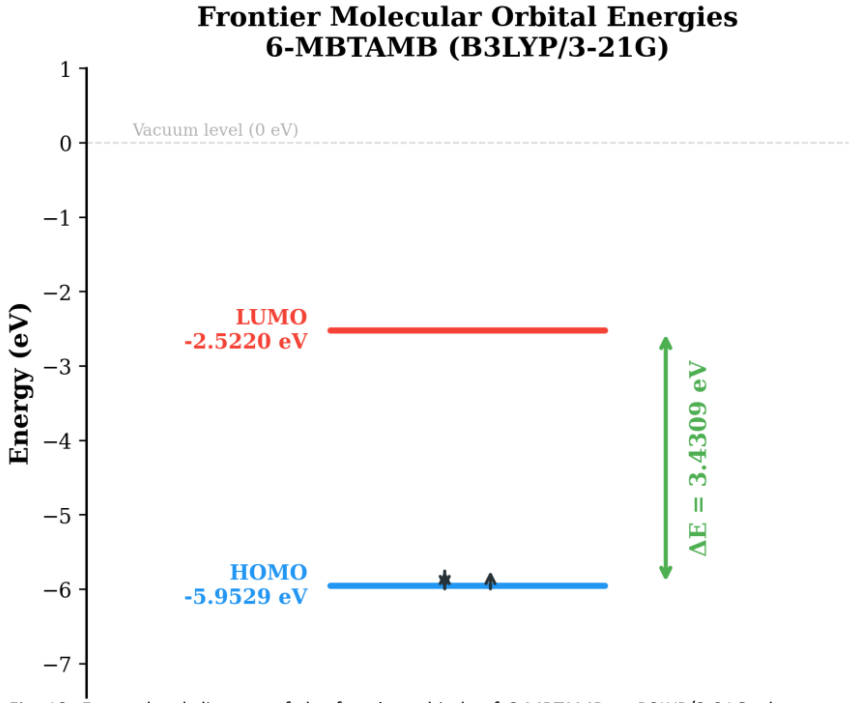


Fig. 13. Energy-level diagram of the frontier orbitals of 6-MBTAMB at B3LYP/3-21G; the arrow marks the HOMO–LUMO gap, ΔE = 3.4309 eV.

Hartree, i.e. −39107.13 eV. There were 178 electrons in the calculation and 250 contracted Gaussian functions to describe them, sufficient for a π-system that extends from the benzothiazole across the azo bridge and into the substituted benzoic acid ring. With the wavefunction settled at this level, the orbital energies and charge analyses discussed next stand on firm ground [37].

*Frontier Molecular Orbital Analysis*

Much of the chemistry of the nano-ligand system can be read off its frontier orbitals. Table 6 and Fig. 13 place the HOMO of 6-MBTAMB at −5.9529 eV and the LUMO at −2.5220 eV, so the gap is ΔE = 3.4309 eV. A gap of this size is typical for a conjugated heterocyclic azo compound: larger than in reactive open-shell species (ΔE < 2 eV), smaller than in kinetically inert saturated molecules (ΔE > 6 eV). The LUMO is fairly low at −2.52 eV, which means the molecule accepts electron density without difficulty; that fits the ease with which it was found to bind Pt(IV) and form the nano-complex. Similar gaps have been published for related chromophores, 2.85–3.08 eV for benzothiazolyl azo-pyrazolone dyes at B3LYP/6-31+G(d) [38] and 3.42 eV for a heterocyclic azo dye ligand at B3LYP/6-311G(d,p) [39], so the value of 3.4309 eV obtained here falls where this class of compound would put it.

*Global Reactivity Descriptors*

Table 6 and Fig. 14 list the global reactivity parameters obtained from the orbital energies through Koopmans' theorem. Oxidation of 6-MBTAMB is only moderately easy (I = 5.9529 eV); accepting electrons comes more naturally to it (A = 2.5220 eV). Electronegativity is high for an organic molecule, χ = 4.2375 eV. Three withdrawing groups act on one π-system here, azo plus thiazole plus carboxylic acid, and the pull accumulates. Hardness lands at η = 1.7154 eV. In HSAB terms that is a soft molecule, and a soft donor suits a soft acceptor; Pt(IV) is exactly that [40].

ω = 5·2336 eV is a large electrophilicity index;

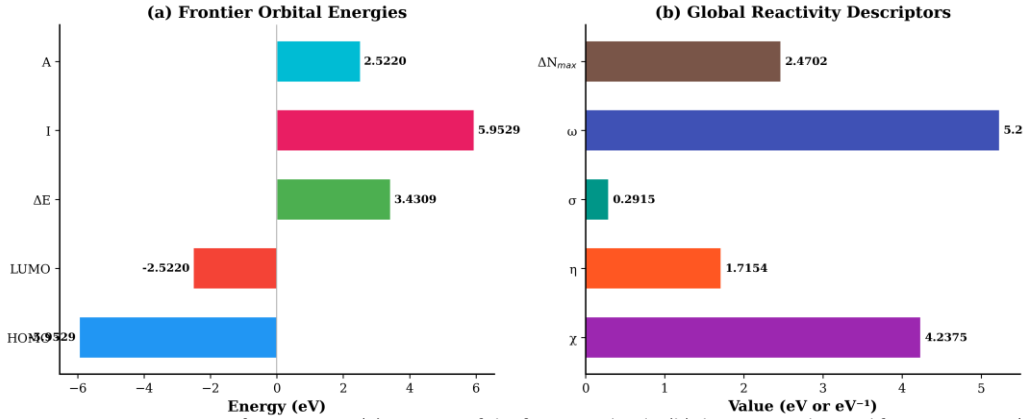


Fig. 14. Reactivity picture of 6-MBTAMB: (a) energies of the frontier orbitals; (b) descriptors obtained from Koopmans' theorem.

Table 6. Frontier-orbital energies of 6-MBTAMB and the global reactivity descriptors derived from them (B3LYP/3-21G).

| Parameter | Symbol | Value |
|---|---|---|
| Total Energy | E | −1437.1389 Ha |
| HOMO energy | $E_{homo}$ | −5.9529 eV |
| LUMO energy | $E_{lumo}$ | −2.5220 eV |
| Energy gap | ΔE | 3.4309 eV |
| Ionization potential | I | 5.9529 eV |
| Electron affinity | A | 2.5220 eV |
| Electronegativity | χ | 4.2375 eV |
| Chemical potential | μ | −4.2375 eV |
| Chemical hardness | η | 1.7154 eV |
| Chemical softness | σ | 0.2915 $eV^{-1}$ |
| Electrophilicity index | ω | 5.2336 eV |
| Maximum charge-transfer index | ΔNmax | 2.4702 |

anything above 1.5 eV already counts as a strong electrophile [41]. Electron density therefore flows toward this ligand whenever a nucleophilic partner is available. Experiment agrees: complexation with Pt(IV) went quickly under mild conditions and gave stable nanoparticles. The charge-transfer estimate ΔN_max = 2.4702 says the ligand could take up about 2.5 electrons in an ideal donor–acceptor pair, and a tridentate (N,N,O) attachment, the mode the spectra indicate, is consistent with that number [42].

*Mulliken Population Analysis*

Mulliken charges are collected in Table 7 and drawn in Fig. 15; the coordination chemistry can almost be read straight off them. S22, the benzothiazole sulfur, holds the largest positive charge in the molecule, +0.7668 e, which comes from its place in the aromatic π-system. The carboxylic carbon C13 follows at +0.6302 e. On either side of C13 sit two negative oxygens, O14 (C=O) at −0.4846 e and O15 (OH) at −0.5501 e. A charge like that on O15 is what qualifies it as a donor atom toward the metal [43].

N9 and N10, the azo nitrogens, carry −0.3152 e and −0.3022 e; π-density from the –N=N– bond accounts for both values. The thiazole nitrogen N7 is more negative still, −0.5129 e, the most nucleophilic nitrogen in the molecule and an obvious σ-donor toward platinum. O2 of the methoxy group also holds substantial charge, −0.5588 e, but it points away from the binding region. Nucleophilic character thus gathers at N7, N9/N10 and O15, and these are the very atoms the NNO tridentate arrangement uses. The stability of the resulting Pt(IV) nano-complex follows naturally [44].

*Molecular Electrostatic Potential Surface*

Projecting the Mulliken charges onto the molecular surface gives the MEP map of Fig. 16. Red, negative regions sit on the carboxylate oxygens, the methoxy oxygen and the thiazole nitrogen: the electron-donating positions. Blue, positive regions surround the sulfur and follow the carbon skeleton. Nothing in the map contradicts

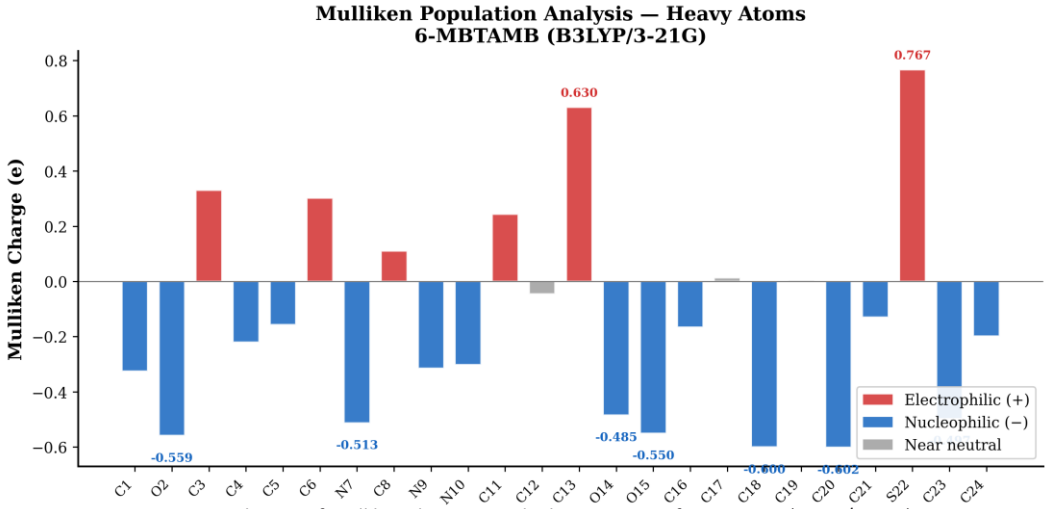


Fig. 15. Distribution of Mulliken charge over the heavy atoms of 6-MBTAMB (B3LYP/3-21G).

Table 7. Mulliken charges computed for the chemically important atoms of 6-MBTAMB (B3LYP/3-21G).

| Atom | Charge (e) | Character |
|---|---|---|
| S22 (thiazole) | +0.7668 | Strong electrophilic |
| C13 (COOH) | +0.6302 | Electrophilic |
| C3 (ring) | +0.3303 | Mild electrophilic |
| N7 (thiazole) | −0.5129 | Strong nucleophilic |
| N9 (azo, =N–) | −0.3152 | Nucleophilic |
| N10 (azo, –N=) | −0.3022 | Nucleophilic |
| O2 (methoxy) | −0.5588 | Strong nucleophilic |
| O15 (OH) | −0.5501 | Strong nucleophilic |

the point-charge analysis; it presents the same conclusion spatially. Platinum binding through the N and O donors, and not through other positions, is what one would predict from this picture, and it is what happens in the stable nano-complex [45].

*TD-DFT UV-Vis Absorption Spectrum*

Ten singlet excited states emerge from the TD-DFT calculation at the TDA-B3LYP/STO-3G level, spread over 260–528 nm (Table 8, Fig. 17). Strongest among them is $S_4$ at λ = 328.1 nm, with oscillator strength f = 0.3919. Its character is mainly π→π*: the electron leaves occupied π-orbitals on the benzothiazole ring system for an antibonding π*-orbital spread across the azo bridge. Transitions at 289.8 nm ($S_6$, f = 0.2329)

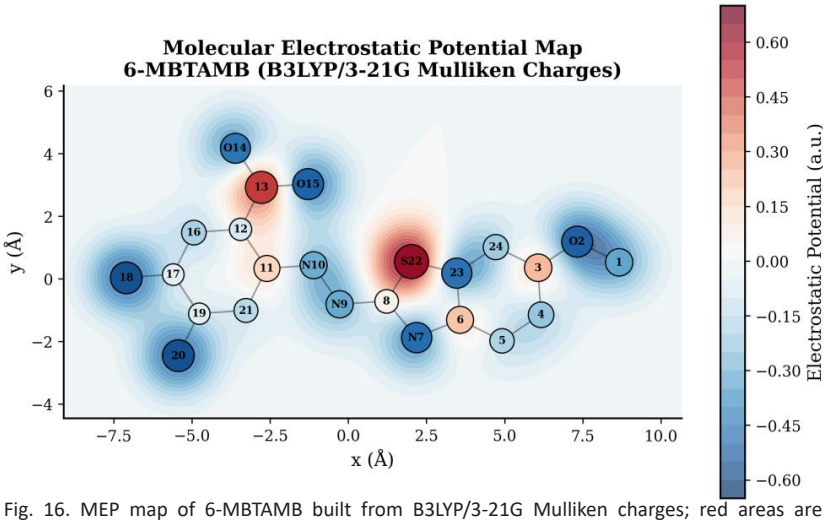


Fig. 16. MEP map of 6-MBTAMB built from B3LYP/3-21G Mulliken charges; red areas are nucleophilic, blue areas electrophilic.

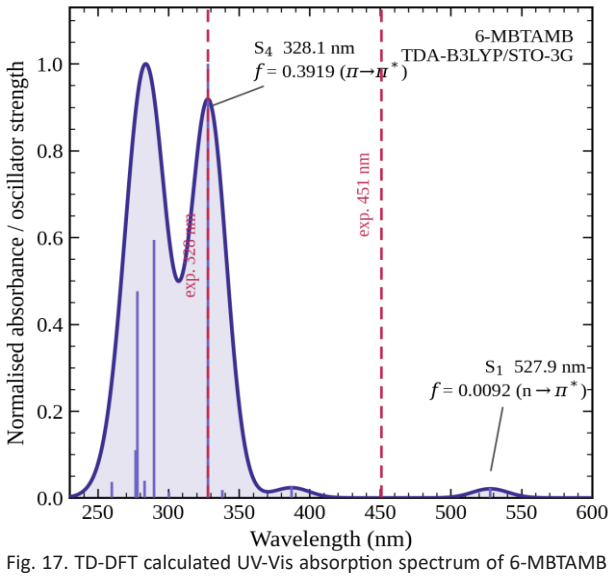


Fig. 17. TD-DFT calculated UV-Vis absorption spectrum of 6-MBTAMB (TDA-B3LYP/STO-3G), Gaussian-broadened with FWHM = 30 nm; vertical bars are the computed oscillator strengths. The experimental absorption maxima of the free ligand (328 and 451 nm, dashed red lines) are shown for comparison, the calculation having been performed on the uncomplexed molecule.

and 278.1 nm ($S_8$, f = 0.1864) carry appreciable strength too, and together these build the broad UV absorption envelope [46].

The lowest-energy excitation ($S_1$, λ = 527.9 nm, f = 0.0092) corresponds to the n→π* transition of the azo chromophore, its very small oscillator strength being characteristic of a symmetry-forbidden excitation. Because the calculation was performed on the uncomplexed molecule, the computed spectrum must be compared with the experimental spectrum of the free ligand rather than with that of the complex. On this basis the agreement for the principal band is excellent: the computed $S_4$ transition at 328.1 nm coincides with the experimental π→π* maximum of 6-MBTAMB at 328 nm (Table 2). The calculated n→π* transition (527.9 nm) is overestimated by roughly 77 nm relative to the experimental value of 451 nm, a well-documented shortcoming of TD-DFT for n→π* excitations that is further amplified here by the minimal STO-3G basis set and by the neglect of solvent (ethanol) effects in the gas-phase model [46,47]. The visible band of the Pt(IV) nano-complex at 496 nm is not directly comparable with either value, since it arises from the metal-centred d–d manifold that is by construction absent from the free-ligand calculation. Notwithstanding the quantitative offset for the forbidden transition, TD-DFT reproduces the overall spectral topology correctly a weak n→π* band in the visible region and intense π→π* transitions at higher energy and provides reliable assignments for the observed

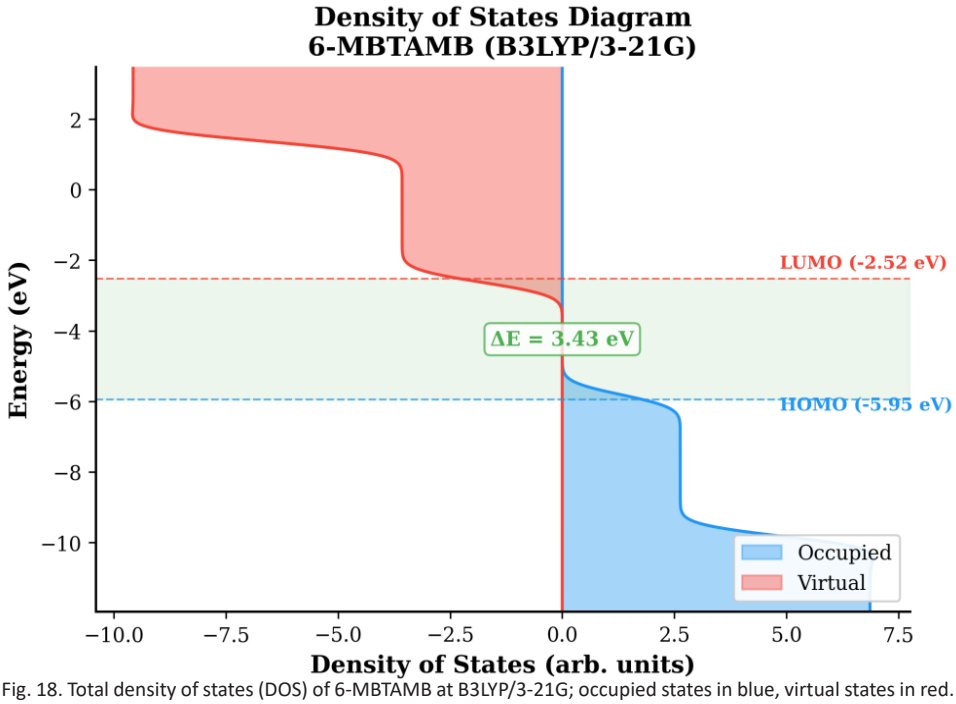


Fig. 18. Total density of states (DOS) of 6-MBTAMB at B3LYP/3-21G; occupied states in blue, virtual states in red.

Table 8. TD-DFT excitation energies and oscillator strengths of 6-MBTAMB (TDA-B3LYP/STO-3G).

| State | λ (nm) | E (eV) | f |
|---|---|---|---|
| S1 | 527.9 | 2.3486 | 0.009150 |
| S2 | 387.2 | 3.2019 | 0.010227 |
| S3 | 338.3 | 3.6649 | 0.006968 |
| S4 | 328.1 | 3.7792 | 0.391892 |
| S5 | 300.3 | 4.1292 | 0.005094 |
| S6 | 289.8 | 4.2781 | 0.232927 |
| S7 | 283.0 | 4.3810 | 0.015555 |
| S8 | 278.1 | 4.4579 | 0.186432 |
| S9 | 276.8 | 4.4789 | 0.043124 |
| S10 | 260.0 | 4.7686 | 0.014272 |

absorptions.

*Density of States Analysis*

The density of states (DOS) diagram (Fig. 18) provides a complementary view of the electronic structure. The occupied DOS shows a dense manifold of states from approximately −12 eV up to the HOMO at −5.95 eV. Above the LUMO at −2.52 eV the virtual states climb steeply. Between the two regions the diagram stays empty, so the 3.43 eV HOMO–LUMO gap can be seen at a glance. The DOS view also anticipates what coordination will do to the spectrum: metal d-orbital states enter the gap when the nano-complex forms, and it is these that permit the LMCT and d–d transitions recorded experimentally [48].

*Proposed Structure of the Pt(IV) Nano-Complex*

Putting the spectroscopic, morphological and computational evidence side by side leads to the following assignment for the Pt(IV) nano-complex. 6-MBTAMB binds as a tridentate (N,N,O) ligand, using the thiazole nitrogen (N7), one azo nitrogen (N9) and the carboxylate oxygen (O15); these three donors take up one face of the octahedron, and three chloride ligands fill the remaining positions. A single water molecule sits in the crystal lattice, which is what the broad O–H stretch in the IR spectrum indicates. The non-electrolytic molar conductance, the diamagnetism and the d–d band pattern all agree on a low-spin octahedral $d^6$ Pt(IV) center with $d^2sp^3$ hybridization. FESEM and XRD, finally, show the compound to be nanoparticulate, with a mean crystallite size of 21.71 nm and a mean particle size of 40.50 nm. On this evidence the formula is $[Pt(L)Cl_3]\cdot H_2O$, where L = 6-MBTAMB bound as a monoanionic tridentate ligand [49]. The proposed structure is depicted in Fig. 19.

*Comparison with Related Azo Dye Ligands and Their Metal Complexes*

To place the present results in context, Table 9 collects frontier-orbital and nanostructural data reported for structurally related azo dye ligands and their metal complexes. Three observations follow. First, the HOMO–LUMO gap computed here for 6-MBTAMB (3.4309 eV) falls within the narrow band of 2.85–3.42 eV reported for benzothiazolyl and other heterocyclic azo chromophores [38,39], indicating that the 6-methoxybenzothiazole–azo–benzoic acid framework possesses the electronic character expected of this family notwithstanding the modest basis set employed. Second, the nanoscale dimensions obtained here are closely paralleled by the nano-azo system of Mohamed et al. [36], in which SEM particle sizes fell from 64–67 nm for the free ligand to 20–32 nm for the Cd(II) complex, and XRD crystallite sizes from 33.78 to 26.77 nm the same direction and very nearly the same magnitude of change as observed here (FESEM 68.89 → 40.50 nm; XRD 29.25 → 21.71 nm). Contraction of the crystalline domain upon coordination therefore appears to be a general characteristic of this class of azo

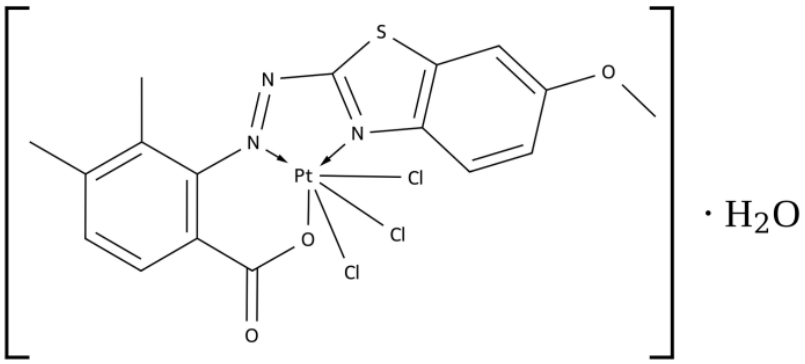


$[Pt(L)Cl_3]\cdot H_2O$ (L = 6-MBTAMB, monoanionic tridentate N,N,O donor)

$C_{17}H_{16}Cl_3N_3O_4PtS$, M.wt. = 659.84 g $mol^{-1}$, octahedral, $d^2sp^3$, diamagnetic

Fig. 19. Proposed structure of the Pt(IV) nano-complex $[Pt(L)Cl_3]\cdot H_2O$, showing the tridentate (N,N,O) coordination of 6-MBTAMB through the thiazole nitrogen, the azo nitrogen and the carboxylate oxygen, three chloride ligands completing the octahedron, and one lattice water molecule outside the coordination sphere.

dye complex rather than a peculiarity of the present preparation. Third, benzothiazole-derived ligands are consistently reported to yield nano-dimensioned complexes with platinum-group and other heavy metals [14,53], which supports the structural assignment advanced above.

A further trend evident in Table 9 is that coordination almost invariably narrows the HOMO–LUMO gap of the free ligand, frequently by 1–2 eV [39,50]. Although the corresponding calculation was not performed for $[Pt(L)Cl_3]\cdot H_2O$ in the present work (see Section 3.13), the pronounced bathochromic shift of the ligand bands observed experimentally upon complexation (328 → 348 nm and 451 → 496 nm) is entirely consistent with such a contraction of the frontier-orbital separation.

*Scope and Limitations of the Computational Model*

Several caveats should be borne in mind when the computational results presented above are interpreted. (i) The DFT and TD-DFT calculations were performed on the free ligand only; the Pt(IV) nano-complex itself was not modelled, because a reliable description of a third-row transition metal requires a relativistic effective core potential (e.g. LANL2DZ or SDD) combined with a polarised valence basis set for the light atoms, which lies beyond the scope of the present study. No calculated HOMO–LUMO gap, Mulliken charge distribution or MEP surface is therefore reported for the complex, and the d–d transitions observed at 496, 441 and 348 nm are assigned on the basis of ligand-field theory rather than from first principles.

(ii) The 3-21G and STO-3G basis sets employed for the ground- and excited-state calculations respectively are of minimal to split-valence quality and carry neither polarisation nor diffuse functions; absolute orbital energies and excitation energies obtained at this level are subject to systematic errors of several tenths of an electronvolt, so the descriptors listed in Table 6 are best read as internally consistent trends rather than as quantitatively converged values [43,47]. (iii) All calculations were carried out in the gas phase on a geometry pre-optimised at the MMFF94 force-field level, whereas the experimental spectra were recorded in ethanol; solvent stabilisation of the more polar excited states typically red-shifts π→π* bands and blue-shifts n→π* bands, which accounts for part of the residual discrepancy discussed in Section 3.10.6. (iv) The MEP surface was reconstructed from Mulliken atomic charges

Table 9. Frontier-orbital energies, HOMO–LUMO gaps and nanoscale dimensions reported for 6-MBTAMB and structurally related azo dye systems.

| Compound | Method | E_HOMO (eV) | E_LUMO (eV) | ΔE (eV) | Size (nm) | Ref. |
|---|---|---|---|---|---|---|
| 6-MBTAMB (free ligand) | B3LYP/3-21G | −5.9529 | −2.5220 | 3.4309 | 29.25 XRD / 68.89 FESEM | This work |
| $[Pt(L)Cl_3]\cdot H_2O$ | not computed (see 3.13) | – | – | – | 21.71 XRD / 40.50 FESEM | This work |
| Benzothiazolyl azo-pyrazolone dyes 3a–3d | B3LYP/6-31+G(d) | n.r. | n.r. | 2.85–3.08 | n.r. | [38] |
| Heterocyclic azo dye ligand ($L^1$) | B3LYP/6-311G(d,p) | −5.27 | −1.85 | 3.42 | n.r. | [39] |
| Cr–Cd complexes of $L^1$ | B3LYP/6-311G(d,p) + LANL2DZ | −3.77 to −8.81 | −1.76 to −6.47 | 1.01–3.28 | n.r. | [39] |
| 1-(4-Nitrophenylazo)-2-naphthol ($HL^2$) | B3LYP/6-311(d,p) | −6.11 | −3.24 | 2.87 | n.r. | [50] |
| Mn–Cu complexes of $HL^2$ | B3LYP/6-311(d,p) + LANL2DZ | −4.09 to −6.16 | −3.39 to −3.60 | 0.70–2.68 | n.r. | [50] |
| Nano-azo ligand $H_2L^3$ | B3LYP/LANL2DZ | −6.095 | −2.977 | 3.349 [a] | 33.78 XRD / 64–67 SEM | [36] |
| $[Cd(H_2L^3)Cl_2]\cdot H_2O$ | B3LYP/LANL2DZ | −5.61 | −4.096 | 1.508 [a] | 26.77 XRD / 20–32 SEM | [36] |
| 2-(Benzothiazol-2-yl)acetamide ($L^4$) | B3LYP/6-311G** | −6.6292 | −1.2481 | 5.3811 | n.r. | [51] |
| Ni/Cu/Zn complexes of $L^4$ | B3LYP/6-311G** + LANL2DZ | −11.74 to −12.16 | −7.30 to −11.69 | 0.45–4.87 | n.r. | [51] |

n.r. = not reported. [a] Values quoted exactly as printed in the source; the tabulated HOMO–LUMO differences are 3.118 and 1.514 eV respectively.

projected onto the molecular framework rather than from the full converged electron density, and is consequently qualitative; Mulliken charges are themselves known to be basis-set dependent [13,43].

A fully relativistic DFT and TD-DFT treatment of $[Pt(L)Cl_3]\cdot H_2O$ at the B3LYP/LANL2DZ U 6-311G(d,p) level, incorporating a continuum solvation model and complemented by molecular docking, represents the natural next step and would allow the coordination-induced changes in electronic structure inferred here to be quantified directly.

## CONCLUSION

A novel heterocyclic azo dye ligand, 6-MBTAMB, was successfully synthesized and coordinated with Pt(IV) to form a mononuclear octahedral nano-complex $[Pt(L)Cl_3]\cdot H_2O$. Elemental analysis together with FT-IR, UV-Vis, $^1$H-NMR, mass spectrometry, powder XRD and FESEM established the identity and purity of both compounds and fixed the binding mode of the ligand as tridentate (N,N,O). FESEM put the mean particle size at 68.89 nm for the ligand and 40.50 nm for the complex, and the XRD crystallite sizes, 29.25 nm and 21.71 nm respectively, told the same story. By either measure the prepared complex is a nano-sized material.

The B3LYP/3-21G calculations gave a quantitative account of the frontier orbitals of the free ligand. The gap, 3.4309 eV, points to moderate kinetic stability; the LUMO lies low, so the molecule takes up electrons readily. By the Koopmans measures ($\omega$ = 5.23 eV, $\eta$ = 1.72 eV) 6-MBTAMB is soft and strongly electrophilic, properties that suit binding to the equally soft Pt(IV) ion. Donor sites identified by the Mulliken charges, namely the thiazole nitrogen, the azo nitrogens and the carboxylate oxygen, coincide with the coordination mode the spectra gave. The TD-DFT spectrum has the right shape as well; its main $\pi\rightarrow\pi^*$ band appears at 328 nm. The nanoscale morphology, combined with the favorable electronic properties revealed by DFT analysis, makes this Pt(IV) nano-complex a promising candidate for further investigation in biomedical, catalytic, and materials science applications.

The lattice microstrain and dislocation density averaged over all observed reflections ($\varepsilon = 6.66 \times 10^{-3}$ and $\delta = 6.36 \times 10^{-3}$ nm$^{-2}$ for the ligand; $\varepsilon = 1.16 \times 10^{-2}$ and $\delta = 1.51 \times 10^{-2}$ nm$^{-2}$ for the complex) independently corroborate the contraction and increased defectiveness of the crystalline domains upon coordination. The computational component of this work is confined to the free ligand; a relativistic DFT treatment of the complex itself, together with an evaluation of its antimicrobial and cytotoxic profile, constitutes the natural continuation of the study.

## ACKNOWLEDGMENTS

The authors gratefully acknowledge the Department of Chemistry, College of Science, University of AL-Qadisiyah for providing laboratory facilities and computational resources.

## CONFLICT OF INTEREST

The authors declare that there is no conflict of interests regarding the publication of this manuscript.

## REFERENCES

1. Benkhaya S, M'Rabet S, El Harfi A. Classifications, properties, recent synthesis and applications of azo dyes. Heliyon. 2020;6(1):e03271.
2. Kumari B, Ahmad K. Barbituric acid-derived azo dye metal complexes: Synthesis, characterization, DFT, and antimicrobial analysis. Appl Organomet Chem. 2024;38(7).
3. Al-Adilee K, Kyhoiesh HAK. Preparation and identification of some metal complexes with new heterocyclic azo dye ligand 2-[2 – - (1- Hydroxy -4- Chloro phenyl) azo ]-imidazole and their spectral and thermal studies. J Mol Struct. 2017;1137:160-178.
4. Tripathy L, Sarangi Ashish K. Synthesis, Characterization, Biological and Computational Insights of some Binuclear Azo Dye-Based Metal Complexes. Appl Organomet Chem. 2025;39(11).
5. Jirjees VY, Al-Hamdan AA. Evaluation of the Antioxidant and Anticancer Effectiveness of Some New Metal Ions Complexes with Azo Dye: Synthesis and Characterization. Indonesian Journal of Chemistry. 2025;25(4):1132.
6. Alshehab A, Haider A, Jaragh-Alhadad L. Significance of Nano Transition Metal Complexes as Anticancer and Antibacterial Therapeutic Agents. Int J Mol Sci. 2025;26(21):10516.
7. Khedr AM, El-Ghamry HA, El-Sayed YS. Nano-synthesis, solid-state structural characterization, and antimicrobial and anticancer assessment of new sulfafurazole azo dye-based metal complexes for further pharmacological applications. Appl Organomet Chem. 2021;36(3).
8. Chuan Lim EW, Feng R. Agglomeration of magnetic nanoparticles. The Journal of Chemical Physics. 2012;136(12).
9. Li X, Liu Y, Tian H. Current Developments in Pt(IV) Prodrugs Conjugated with Bioactive Ligands. Bioinorg Chem Appl. 2018;2018:1-18.
10. Kyhoiesh HAK, Al-Adilee KJ. Synthesis, spectral characterization and biological activities of Ag(I), Pt(IV) and Au(III) complexes with novel azo dye ligand (N, N, O) derived from 2-amino-6-methoxy benzothiazole. Chemical Papers. 2022;76(5):2777-2810.

11. Calais JL. Density-functional theory of atoms and molecules. R.G. Parr and W. Yang, Oxford University Press, New York, Oxford, 1989. IX + 333 pp. Price £45.00. International Journal of Quantum Chemistry. 1993;47(1):101-101.
12. U R, Nehal SK, N. M M, K V, S. M AK, H. M SK, et al. Computational and Spectroscopic Study of Newly Synthesized Bio-Active Azo Dyes: DFT, Solvatochromism, and Preferential Solvation. ChemistrySelect. 2024;9(48).
13. Mulliken RS. Electronic Population Analysis on LCAO–MO Molecular Wave Functions. I. The Journal of Chemical Physics. 1955;23(10):1833-1840.
14. Kyhoiesh HAK, Al-Adilee KJ. Pt(IV) and Au(III) complexes with tridentate-benzothiazole based ligand: synthesis, characterization, biological applications (antibacterial, antifungal, antioxidant, anticancer and molecular docking) and DFT calculation. Inorg Chim Acta. 2023;555:121598.
15. Al-Adilee KJ, Kyhoiesh HAK, Taher AM. Synthesis, characterization, biological studies, molecular docking and theoretical calculation of some transition metal complexes with new azo dye 2-[2'-(6-methoxybenzothiazolyl)azo]-3-methyl-4-nitrophenol. Results in Chemistry. 2022;4:100500.
16. Geary WJ. The use of conductivity measurements in organic solvents for the characterisation of coordination compounds. Coord Chem Rev. 1971;7(1):81-122.
17. Sun Q, Berkelbach TC, Blunt NS, Booth GH, Guo S, Li Z, et al. P y SCF: the Python-based simulations of chemistry framework. WIREs Computational Molecular Science. 2017;8(1).
18. Koopmans T. Über die Zuordnung von Wellenfunktionen und Eigenwerten zu den Einzelnen Elektronen Eines Atoms. Physica. 1934;1(1-6):104-113.
19. Ríos-Gutiérrez M, Saz Sousa A, Domingo LR. Electrophilicity and nucleophilicity scales at different DFT computational levels. J Phys Org Chem. 2023;36(7).
20. Al-Adilee KJ, Abass AK, Taher AM. Synthesis of some transition metal complexes with new heterocyclic thiazolyl azo dye and their uses as sensitizers in photo reactions. J Mol Struct. 2016;1108:378-397.
21. Gliemann G. A. B. P. Lever: Inorganic Electronic Spectroscopy, Vol. 33 aus: Studies in Physical and Theoretical Chemistry, Elsevier, Amsterdam, Oxford, New York, Tokio 1984. 863 Seiten, Preis: $ 113, 50. Berichte der Bunsengesellschaft für physikalische Chemie. 1985;89(1):99-100.
22. Kowey PR. Novel Therapeutic Targets for Antiarrhythmic DrugsBillmanGeorge Edward ed. 573 pages. Hoboken, NJ, USA: John Wiley and Sons, Inc, 2010. $149.95. ISBN: 978-0-470-26100-2. Circulation. 2011;123(7).
23. Jawad SH, Al-Adilee KJ. Synthesis, spectroscopic characterization and biological activities as an anticancer and antioxidant of the Pd(II) and Pt(IV) complexes with a new azo dye ligand derived from 5-methyl imidazole. J Mol Struct. 2023;1277:134846.
24. Rose ME. Interpretation of mass spectra, 4th edition F. W. McLAFFERTY AND F. TUREČEK Published by University Science Books, Mill Valley, 1993 ISBN 0-935702-25-3, xiii + 371 pp. Rapid Commun Mass Spectrom. 1994;8(6):501-501.
25. Falah NS, Abdullaha SAH, Jabir MS. New azo derivative and their divalent metal ion complexes: Synthesis, characterization, and evaluation of their antibacterial activity. J Indian Chem Soc. 2023;100(6):101010.
26. Bellamy LJ. The Infra-red Spectra of Complex Molecules. Springer Netherlands; 1975.
27. Nakamoto K. Infrared and Raman Spectra of Inorganic and Coordination Compounds: Wiley; 2008 2008/04/30.
28. Fouda MFR, Abd-Elzaher MM, Shakdofa MM, El-Saied FA, Ayad MI, El Tabl AS. Synthesis and characterization of a hydrazone ligand containing antipyrine and its transition metal complexes. J Coord Chem. 2008;61(12):1983-1996.
29. Partee M. An Introduction to Christian Ethics by Robert H. Crook (3rd ed. Upper Saddle River, NJ: Prentice-Hall, 1999. 290 pp., pb. ISBN 0-13095131-5). Evangelical Quarterly. 2002;74(1):82-85.
30. Mukherjee P, Sarkar A, Barat P, Bandyopadhyay SK, Sen P, Chattopadhyay SK, et al. Deformation characteristics of rolled zirconium alloys: a study by X-ray diffraction line profile analysis. Acta Mater. 2004;52(19):5687-5696.
31. Leoni M, Di Maggio R, Polizzi S, Scardi P. X-ray Diffraction Methodology for the Microstructural Analysis of Nanocrystalline Powders: Application to Cerium Oxide. J Am Ceram Soc. 2004;87(6):1133-1140.
32. Scardi P. Chapter 13. Microstructural Properties: Lattice Defects and Domain Size Effects. Powder Diffraction: Royal Society of Chemistry; 2008. p. 376-413.
33. Giannuzzi LA. Scanning Electron Microscopy and X-Ray Microanalysis 4th Edition, Joseph I. Goldstein, Dale E. Newbury, Joseph R. Michael, Nicholas W.M. Ritchie, John Henry J. Scott, David C. Joy, Springer, 2018, 550 pp. ISBN:978-1-4939-6674-5. Microscopy and Microanalysis. 2018;24(6):768-768.
34. Uvarov V, Popov I. Metrological characterization of X-ray diffraction methods for determination of crystallite size in nano-scale materials. Mater Charact. 2007;58(10):883-891.
35. Hampel G, Pundt A, Hesse J. Crystallization of $Fe_{73.5}Cu_1Nb_3Si_{13.5}B_9$ structure and kinetics examined by X-ray diffraction and Mossbauer effect spectroscopy. J Phys: Condens Matter. 1992;4(12):3195-3214.
36. Mohamed GG, Mahmoud WH, Refaat AM. Nano-Azo Ligand and Its Superhydrophobic Complexes: Synthesis, Characterization, DFT, Contact Angle, Molecular Docking, and Antimicrobial Studies. Journal of Chemistry. 2020;2020:1-19.
37. Mousa I, Madkhali Marwah MM, Siddiq Hind A, Alaghaz ANasser MA, Rezk Ghada N, El-Bindary Ashraf A. Synthesis, Characterization, DFT Calculations, and Pharmacological Activity of Azo Dye Ligand and Its Cu(II) Complex Comprising Nitrogen and Oxygen Donor Atoms. Appl Organomet Chem. 2024;39(2).
38. Aktan E, Uyar T. Hetarylazopyrazolone Dyes Based on Benzothiazole and Benzimidazole Ring Systems: Synthesis, Spectroscopic Investigation, and Computational Study. Journal of Chemistry. 2017;2017:1-10.
39. Al-Gaber MAI, Abd El-Lateef HM, Khalaf MM, Shaaban S, Shawky M, Mohamed GG, et al. Design, Synthesis, Spectroscopic Inspection, DFT and Molecular Docking Study of Metal Chelates Incorporating Azo Dye Ligand for Biological Evaluation. Materials. 2023;16(3):897.
40. Pearson RG. Hard and Soft Acids and Bases. Journal of the American Chemical Society. 1963;85(22):3533-3539.
41. Pal R, Chattaraj PK. Electrophilicity index revisited. J Comput Chem. 2022;44(3):278-297.
42. Reed AE, Curtiss LA, Weinhold F. Intermolecular interactions from a natural bond orbital, donor-acceptor viewpoint. Chem Rev. 1988;88(6):899-926.
43. Menzies D. Nick Collins, Introduction to Computer Music. Chichester: John Wiley and Sons, 2010. ISBN 978-0-470-

71455-3. Organised Sound. 2010;15(2):180-181.
44. Politzer P, Murray JS. The fundamental nature and role of the electrostatic potential in atoms and molecules. Theoretical Chemistry Accounts: Theory, Computation, and Modeling (Theoretica Chimica Acta). 2002;108(3):134-142.
45. Althobaiti M, Hermi S, Alotaibi A, Alotaibi K, Hassan H, Mi J-X, et al. A New Cu(II) Metal Complex Template with 4–tert–Butyl-Pyridinium Organic Cation: Synthesis, Structure, Hirshfeld Surface, Characterizations and Antibacterial Activity. Crystals. 2022;12(2):254.
46. Adamo C, Jacquemin D. The calculations of excited-state properties with Time-Dependent Density Functional Theory. Chem Soc Rev. 2013;42(3):845-856.
47. Laurent AD, Jacquemin D. TD-DFT benchmarks: A review. International Journal of Quantum Chemistry. 2013;113(17):2019-2039.
48. Hoffmann R. A chemical and theoretical way to look at bonding on surfaces. Rev Mod Phys. 1988;60(3):601-628.
49. Tocher DA. Advanced Inorganic Chemistry. F. Albert Cotton, Geoffrey Wilkinson, Carlos A. Murillo and Manfred Bochmann. 6th edn. John Wiley and Sons, Chichester, 1999 xv+1353 pages. 58.50 ISBN 0-471-19957-5. Appl Organomet Chem. 2000;14(3):172-173.
50. Alghuwainem YAA, El-Lateef HMA, Khalaf MM, Amer AA, Abdelhamid AA, Alzharani AA, et al. Synthesis, DFT, Biological and Molecular Docking Analysis of Novel Manganese(II), Iron(III), Cobalt(II), Nickel(II), and Copper(II) Chelate Complexes Ligated by 1-(4-Nitrophenylazo)-2-naphthol. Int J Mol Sci. 2022;23(24):15614.
51. Abd El-Nasser MG, Ismail TI. Synthesis, characterization, molecular docking studies, and theoretical calculations of novel Ni (II), Cu (II), and Zn (II) complexes based on benzothiazole derivative. BMC Chemistry. 2025;19(1).
52. Williamson GK, Smallman RE. III. Dislocation densities in some annealed and cold-worked metals from measurements on the X-ray debye-scherrer spectrum. Philos Mag. 1956;1(1):34-46.
53. Alenazy Deemah M, Siddiq Hind A, Alatawi Nada M, Ageeli Abeer A, Alkhathami Nada D, Mousa I, et al. Synthesis, DFT, Spectral Characterization, Cell Cycle, Apoptosis, Cytotoxicity, DNA Binding/Cleavage, Molecular Docking, and Antimicrobial Insights of Nano-Sized Pd (II) and Cu (II) Complexes With Benzothiazole-Appended Ligand. Appl Organomet Chem. 2025;39(6).